Cobalt-doped ZnS-reduced graphene oxide nanocomposite as an advanced photocatalytic material

Eric Selorm Agorku · Messai Adenew Mamo ·
Bhekie Brilliance Mamba · Avinash Chandra Pandey ·
Ajay Kumar Mishra

Abstract The removal of toxic organic pollutants from wastewater by graphene-based photocatalysts has dominated recent scientific research. As a result numerous nanomaterials have been studied and used for water remediation. ZnS has been widely studied due to its versatile application in photocatalysis. This study presents the synthesis of Co-doped graphene–ZnS nanocomposite by co-precipitation method. The materials were characterized by X-ray diffraction , Raman spectroscopy, Fourier transform infrared spectroscopy, scanning electron microscopy, transmission electron microscopy and Brunauer–Emmett–Teller surface area analysis. UV/Vis diffuse reflectance spectroscopy was employed to estimate band gap energies. Laboratory experiments with indigo carmine (IC) dye was chosen as a model for organic pollutants and was used to evaluate the photocatalytic performance of Co-doped ZnS–rGO nanocomposite under visible light. The Co-doped ZnS–rGO showed significant visible light induced photocatalytic activity towards the degradation of IC. Highest photocatalytic activity was observed for the 0.3 % Co-doped ZnS–rGO sample ($k = 3.1 \times 10^{-2}$ min^{-1}).

E. S. Agorku · M. A. Mamo · A. K. Mishra (✉)
Department of Applied Chemistry, University of Johannesburg,
Doornfontein Campus, PO Box 17011, Johannesburg 2028,
South Africa
e-mail: ajaykmishra1@gmail.com; amishra@uj.ac.za

B. B. Mamba
Nanotechnology for Water Sustainability Research Unit,
College of Engineering, Science and Technology, University
of South Africa, Florida Campus, Roodepoort, Johannesburg,
South Africa

A. C. Pandey
Nanotechnology Application Centre, University of Allahabad,
Allahabad 211002, India

1 Introduction

Dyes and pigments have been a subject of much interest in recent years, since the removal of these compounds from wastewater is of great importance [1]. Many of the dyes and their degradation products are toxic and carcinogenic, posing serious hazards to man and the environment [2–4]. As a result, efforts have been directed towards the search for an appropriate treatment technique in order to remove these pollutants from contaminated water.

Many researchers have studied different techniques for the removal of dyes from wastewater, including nanofiltration [5, 6], coagulation/flocculation [7, 8], micellar enhanced ultrafiltration [9], oxidation [10–12], ozonolysis [13–15], the use of activated carbon [16, 17] and biological treatment techniques [18, 19]. However, these conventional wastewater treatment techniques are either expensive or a lot of wastes are generated during the purification process, which limits their application. As a result, many studies are directed towards an efficient treatment process, with photocatalysis gaining much attention in this regard. This method is based on the generation of hydroxyl radicals which attack organic pollutants leading to progressive degradation and its complete mineralization [20, 21].

Over the past few decades, photocatalysis of semiconducting inorganic solids have attracted much interest for the degradation of organic pollutants, including dyes [22, 23]. Semiconductors such as TiO_2, ZnO, Fe_2O_3, CdS and ZnS are proved to be efficient photocatalysts due to their unique chemical and electronic structure. ZnS, a group II–VI semiconductor, is having great interest and have been

widely used in photocatalysis [24–28]. However, its wide bandgap (3.60 eV) prevents its photocatalytic application in the visible-light region. The use of a photocatalyst material having visible-light activity is required for harnessing the full potential of sunlight in wastewater treatment. It is therefore of great significance to adjust the band structure of photocatalysts to improve its photocatalytic efficiency towards the utilization of solar energy. Various attempts such as dye sensitization, coupling with different semiconductors, and doping with metals or nonmetals are performed to modify the bandgap of semiconducting photocatalysts [29–32].

Recently, graphene-inorganic nanocomposites have been intensively developed, and found to exhibit a range of unique properties. With its unique small bandgap, the preparation of a graphene oxide based semiconductor nanocomposite provides a highly efficient visible-light driven photocatalyst for wastewater treatment. Because of its high optical, thermal and mechanical properties, the addition of a graphene oxide to an inorganic semiconductor has the tendency to reveal synergism of properties of the individual materials.

In this study, a series of Co doped ZnS–rGO nanocomposites were synthesized by co-precipitation method. The photocatalytic activity of the nanocomposites for the degradation of indigo carmine (IC) dye in water were discussed.

2 Experimental

All chemicals were obtained from Sigma-Aldrich and used without further purification.

2.1 Synthesis of graphene oxide

Graphite oxide (GO) was prepared starting with natural graphite powder using the modified Hummers method [33]. A 9:1 mixture of concentrated H_2SO_4/H_3PO_4 (360:40 mL) was added to a mixture of graphite flakes (3.0 g, 1 wt equiv) and $KMnO_4$ (18.0 g, 6 wt equiv). The reaction mixture was then heated to 50 °C and stirred for 12 h. After, the reaction mixture was cooled to room temperature. DI water (400 mL) and 30 % H_2O_2 (3 mL) were added slowly. The solution was centrifuged (7,500 rpm for 20 min at 4 °C), and the supernatant was decanted away. The remaining solid material was then washed repeatedly with a total of 1,000 mL of DI water and 30 % HCl. Finally the solid material was dispersed in 1,000 ml of DI water and centrifuged. The remaining material was coagulated with petroleum ether (200 mL) and filtered through a 1 μm pore size Teflon membrane filter. The solid obtained was vacuum-dried overnight at room temperature.

2.2 Reduction of graphene oxide

The procedure for the reduction of the GO was adapted from Fernandez-Merino et al. [34]. Deoxydation of GO was conducted by dispersing the prepared GO at concentration of 0.1 mg L^{-1} in DI water. The pH of the mixture was adjusted to between 9 and 10 with 25 % ammonium solution to promote the colloidal stability of the GO sheets through electrostatic repulsion. After, the solution was sonicated for about 1 h. Vitamin C (2 mmol) was added as a reducing agent and the mixture heated at 95 °C under continuous stirring for 12 h. After 15 min the brown mixture started to turn dark. The reduced grapheme oxide was filtered with 1 μm pore size Teflon membrane filter and washed repeatedly with warm DI water. Finally the reduced graphene oxide was dried under vacuum at room temperature for 24 h or re-dispersed in DI water for use.

2.3 Preparation of Co–ZnS–rGO nanocomposite

An amount of rGO and $CoCl_2$ were dispersed in 50 mL DI water by sonication so that the Zn:Co was 0.3, 0.6 and 1.0 %. The amount of rGO in the entire ZnS matrix was 0.5 %. Then 0.1 M zinc nitrate (10 mL) was added and the mixture stirred magnetically at 50 °C for 2 h. The Co–ZnS–rGO was prepared by adding 0.1 M $Na_2S.9H_2O$ (5 mL) to the mixture drop wise while stirring vigorously on a magnetic stirrer. Co–ZnS–rGO composite were separated by centrifugation after washing several times with DI water and ethanol to remove nitrate and chloride ions. The Co–rGO/ZnS precipitate was dried at 90 °C overnight. ZnS and ZnS–rGO were synthesized in a similar manner without the addition of either $CoCl_2$ or both rGO and $CoCl_2$.

2.4 Evaluation of photocatalytic activity

The photocatalytic activity of the materials was evaluated through a suspension of 100 mg of the catalyst in 100 mL of aqueous solution of IC (20 mg/L) that was kept under magnetic stirring and simulated solar light at room temperature. The suspension was kept under magnetic stirring in the dark for about 1 h prior to illumination with light filtered with a dichroic UV filter ($\lambda > 420$ nm) at room temperature. In order to emulate the sun's energy, a New Port 9600 Full Spectrum Solar Simulator equipped with 150 W ozone free xenon lamp which produces a collimated beam of 33 mm diameter (equivalent to 1.3 sun) was used to study the photodegradation and the kinetic studies of the dyes. In this work, the distance between the simulator and the experimental setup was set at a distance of 10 cm to produce a beam power equivalent to 1 sun. Aliquots of the suspension (5 mL) were withdrawn using disposable

syringe and filtered through 0.4 µm PVDF membrane filter at 30 min intervals for about 4 h. The concentration of the IC remaining after illumination in the supernatant solution was determined using a Shimadzu UV-2450 spectrophotometer at $\lambda = 610$ nm. The photodegradation performance of the process was assessed in terms of decolorization efficiencies and kinetic studies.

2.5 Characterization

Fourier transform infrared spectroscopy (FTIR) spectra of the samples were recorded on PerkinElmer FTIR spectrometer (Spectrum 100). Raman spectra of rGO was measured on PerkinElmer Raman microscope (Raman Micro 200). X-ray diffraction (XRD) measurements were performed on X-ray diffractometer (Rigagu Ultima IV) at 40 kV and 30 mA with Cu Kα radiation ($\lambda = 0.15406$) with K-beta filter. Measurements were performed using a scintillation counter in the range of 5–90° at a speed of 2.0 deg/min. Scanning electron microscopy (SEM) studies were obtained on a TESCAN (Vega 3 XMU) to observe the surface morphology of the powders and transmission electron spectroscopy (TEM) analysis was performed on a JEOL field emission electron microscope (JEM-2100F) to observe the surface morphology, structure, and grain size of the nanoparticles. Eenergy dispersed X-ray spectroscopy (EDX) attached to the SEM was used to determine the surface elemental composition. Brunauer–Emmett–Teller (BET) surface area measurements were performed on a Micromeritics ASAP 2020 instrument. The samples were degassed in a vacuum at 150 °C for 1 h reaching a final pressure of 1 mmHg prior to analysis. Optical properties were investigated using UV–vis absorption and UV–vis diffuse reflectance spectroscopy on a Shimadzu UV-2540 (Japan). BaSO$_4$ was used as the reflectance standard.

3 Results and discussion

3.1 XRD patterns

The XRD patterns of ZnS, rGO and Co-doped ZnS–rGO (with different concentrations of Co) nanoparticles are shown in Fig. 1. The three broad peaks observed in the diffractogram at around 29.0°, 48.2° and 56.7° reveals a face centred cubic structure of zinc sulfide (zincblende). These peaks could be assigned to the planes (111), (220) and (331) respectively of the cubic phase [35] of ZnS (JCPDS No. 05-0566). The broadening in the XRD patterns clearly indicates the formation of nanocrystalline small size of ZnS, rGO and Co-doped ZnS–rGO [36]. The increase in the angle of diffraction is as a result of lattice contraction due to higher surface to volume ratio [37]. However, no
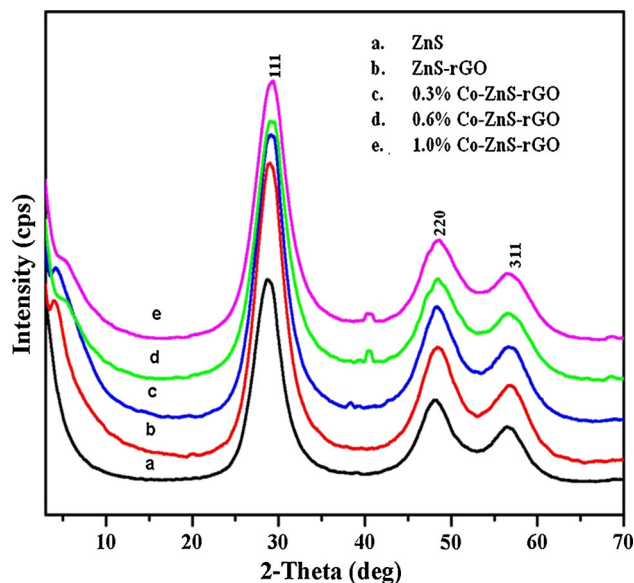
Fig. 1 XRD patterns of ZnS, ZnS–rGO and Co-doped ZnS–rGO with different concentrations of Co

intense observable diffraction peaks for rGO were observed in the ZnS–rGO nanocomposite, and this may be due to the low amount (0.5 %) and relatively low diffraction intensities of rGO in the nanocomposite [38]. The crystalline size of the samples were calculated using the Debye–Shrerres' equation:

$$D = \frac{K\lambda}{\beta \mathrm{Cos}\theta} \tag{1}$$

where D is the crystal size of the catalyst, λ the X-ray wavelength, β the full width at maximum (FWHM) of the diffraction peak (radian), K is a constant (0.89) and θ is the diffraction angle at the maximum. The average crystalline size of the samples were calculated to be between 3 and 5 nm with an average of 3.3 nm.

3.2 FTIR Analysis

The FTIR spectrum provides information on the surface chemistry of nanoparticles which are usually affected by hydration layers. Figure 2 shows the FTIR spectra of the rGO, ZnS, ZnS–rGO and Co-doped ZnS–rGO nanoparticles. In general, the peaks observed between 1,620 and 1,635 cm^{-1} and 3,350 and 3,450 cm^{-1} are due to the bending vibrations of adsorbed water molecules and stretching vibrations from hydroxyl groups respectively. The rGO FTIR spectrum (Fig. 2a) showed characteristic peaks which can be assigned as follows: the stretching vibration peaks of C–O (epoxy) and C–O (alkoxy) are observed at 1,410 and 1,223 cm^{-1} respectively. The presence of alkoxy and epoxy groups in the sample indicates
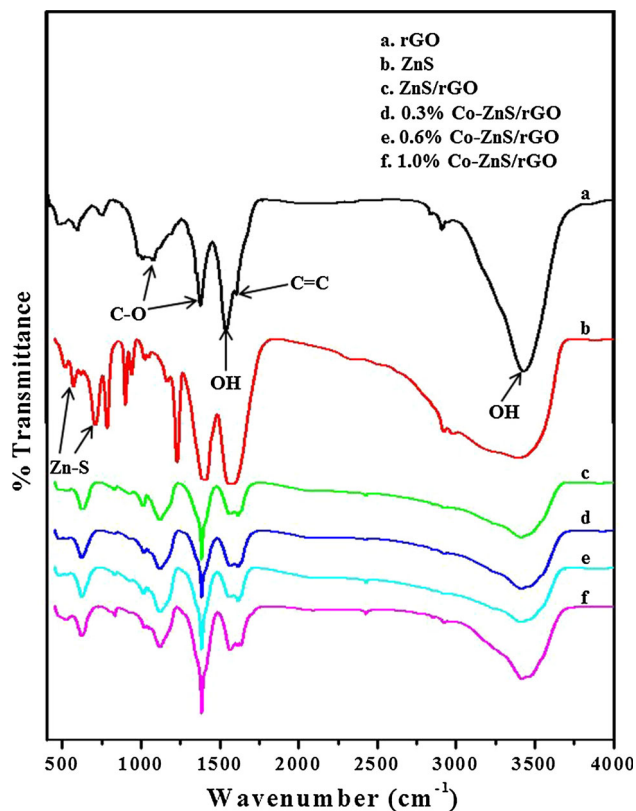
Fig. 2 FTIR spectra of ZnS, ZnS–rGO and Co-doped ZnS–rGO with different concentrations of Co

Fig. 3 Raman spectrum of rGO

the presence of residual oxygen on the rGO. The peak between 1,620 and 1,635 cm^{-1} can be attributed to in plane C=C band and vibrations of aromatic groups of rGO [39]. Notably, all the above peaks were observed for the ZnS–rGO and Co-doped ZnS–rGO (Fig. 2c–f) except that they are slightly shifted to the lower frequency. This could be attributed to the interaction between rGO and ZnS in the composites. Fig. 2b shows the FTIR spectrum of the as-prepared ZnS nanoparticles. The absorptions at ∼560 and 672 cm^{-1} are attributed to stretching vibrations of ZnS bonds [40], which shifted to lower wavenumbers in the nanocomposites indicating the interaction between rGO, Co and ZnS.

3.3 Raman spectroscopy analysis

The formation of rGO was also confirmed by Raman analysis. Raman active fundamental modes for rGO are depicted in Fig. 3. The Raman spectrum of rGO which appeared at 1,351 and 1,587 cm^{-1} corresponds to D and G bands respectively. The G band is due to the first-order scattering of the E_{2g} mode of sp^2-bonded carbon atoms in a 2D hexagonal lattice of graphite whereas the D band response which originates from the edges can be attributed
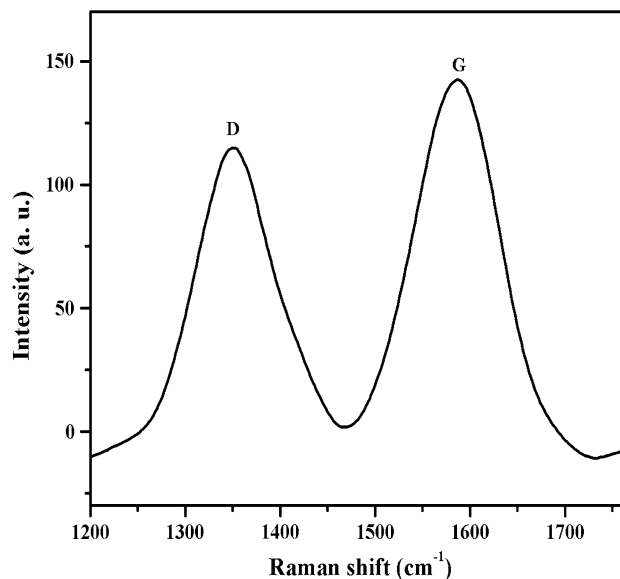
to either defects or breakdown of translational symmetry [41, 42]. However, the relative intensities of D band compared to G band depend strongly on the amount of disorder in the graphitic material [42]. The calculated D/G intensity ratio of rGO (I_G/I_D) in this work is 0.82, demonstrating the reduction of GO.

3.4 TEM and SEM studies

TEM and SEM were performed to assess the size, uniformity, morphology and microstructure of the nanoparticles. The TEM and SEM micrographs of 0.3 % Co-doped ZnS–rGO photocatalysts are shown in Fig. 4a, c respectively. The TEM images revealed that the nanocomposites were small in size with slightly spherical shapes with distinct grain boundaries. The monograph shows that the samples are crystalline in shape after heat treatment in air. All the nanocomposites exhibited regular morphology irrespective of the amount of Co doping.

The elemental composition of the prepared samples was estimated by EDS analyses. Figure 4d shows the EDS spectrum of 0.3 % Co-doped ZnS–rGO. The spectrum of the Co-doped ZnS–rGO confirms the presence of Co, Zn, C, O and S. The spectrum indicates that the main components are Zn and S with low contents of Co, C and O.

3.5 BET surface area analysis

In general, a photocatalyst with high specific surface area and large pore volume has the aptitude to adsorb a variety of organic pollutants and concentrate it on its surface for

Fig. 4 TEM image of 0.3 % Co-doped ZnS–rGO (**a**), TEM image of ZnS (**b**), SEM image of 0.3 % Co-doped ZnSrGO (**c**), and EDS spectrum of 0.3 % Co-doped ZnS–rGO (**d**)
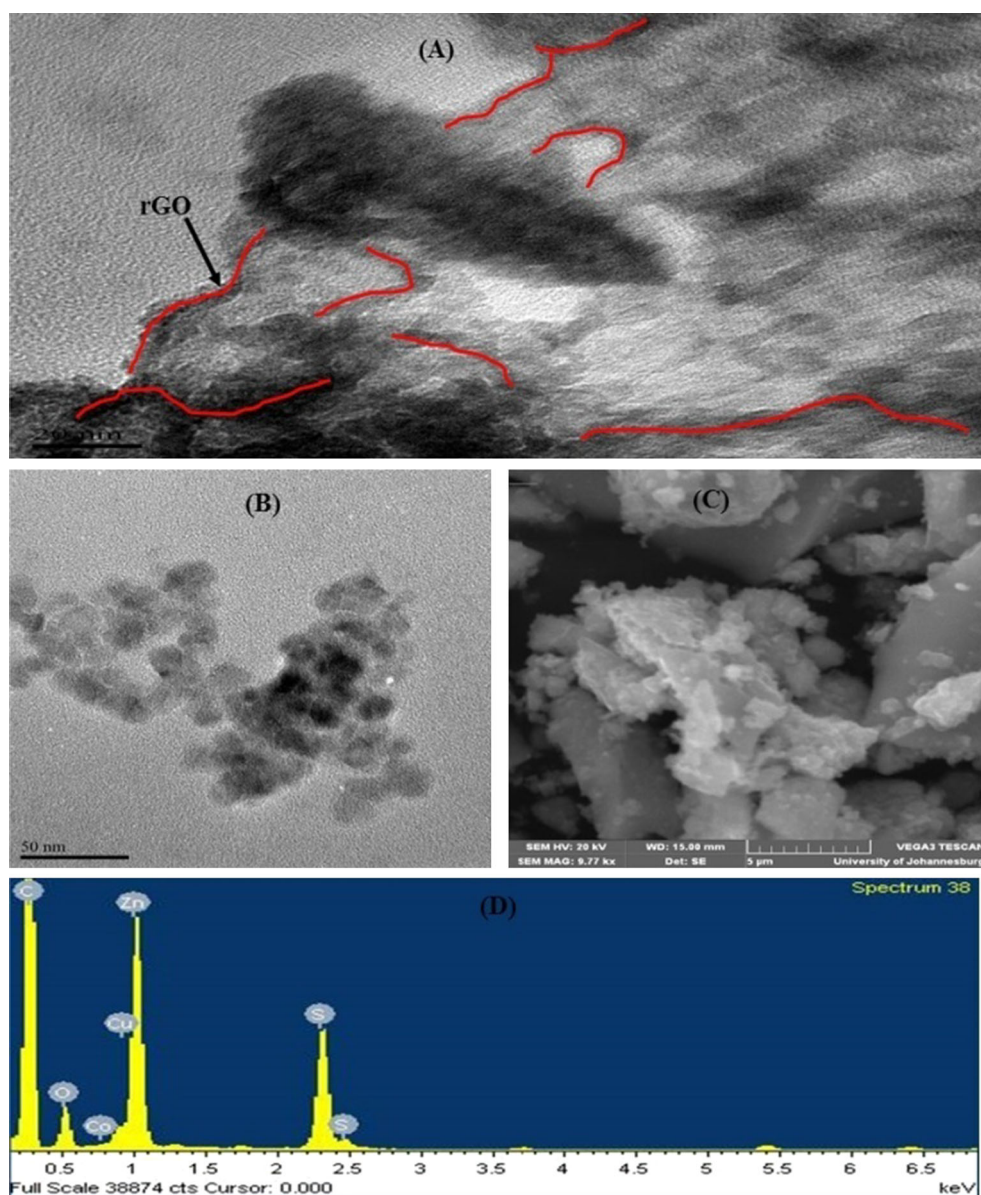
**Table 1** BET surface area, pore volume and pore size

Sample	BET surface area (m^2/g)	Pore volume (cm^3/g)	Pore size (Å)
ZnS/rGO	80.1	0.091	46
0.3 % Co–ZnS/rGO	84.4	0.088	42
0.6 % Co–ZnS/rGO	49.0	0.063	52
1.0 % Co–ZnS/rGO	54.1	0.055	41

enhance photocatalytic performance. The effect of Co doping on the pore size, pore volume and BET surface areas of the nanocomposites was investigated by the adsorption–desorption measurement (Table 1). There was no correlation between Co doping and surface area of the nanocomposites. The ZnS–rGO and Co-doped ZnS–rGO samples showed an increase in the BET surface area, pore size and pore volume compared with the bare ZnS nanoparticle. The increase in surface area of the nanocomposites could be useful in the photocatalytic process which might result in an efficient transport of the pollutants in the solution to the surface of the photocatalyst for an enhance photocatalytic degradation.

3.6 Optical studies

The UV–visible absorption analysis of the samples (Fig. 5) reveal that chemical modification of ZnS was achieved by using rGO and Co. Cubic ZnS is known to have a wide bandgap (ca. 3.60 eV) [40] and as a result it cannot be
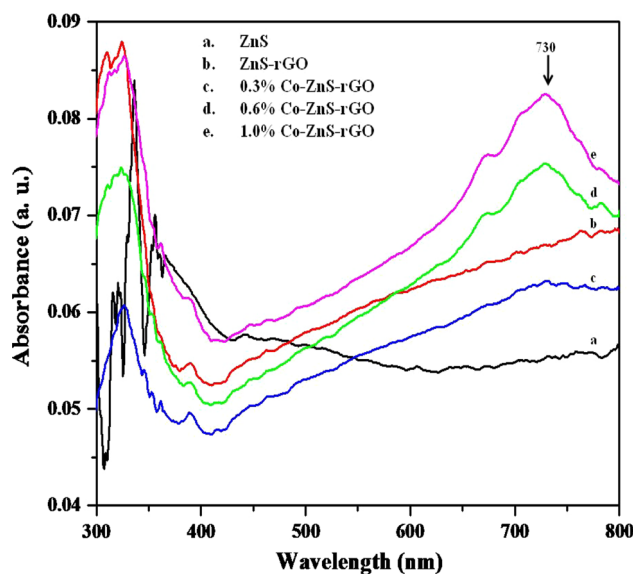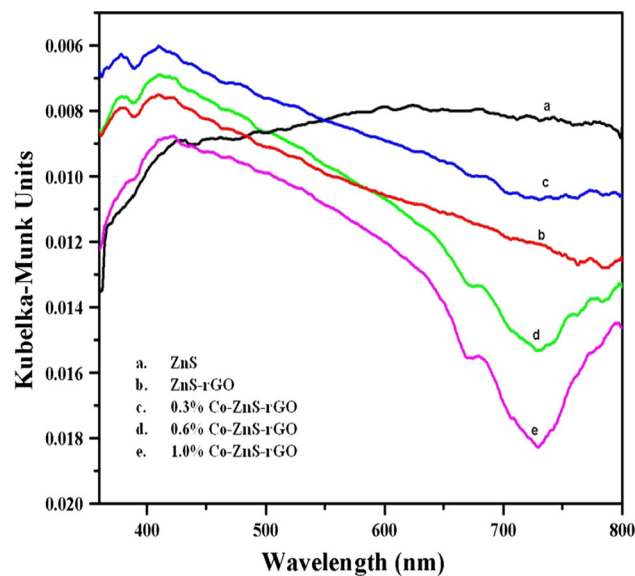
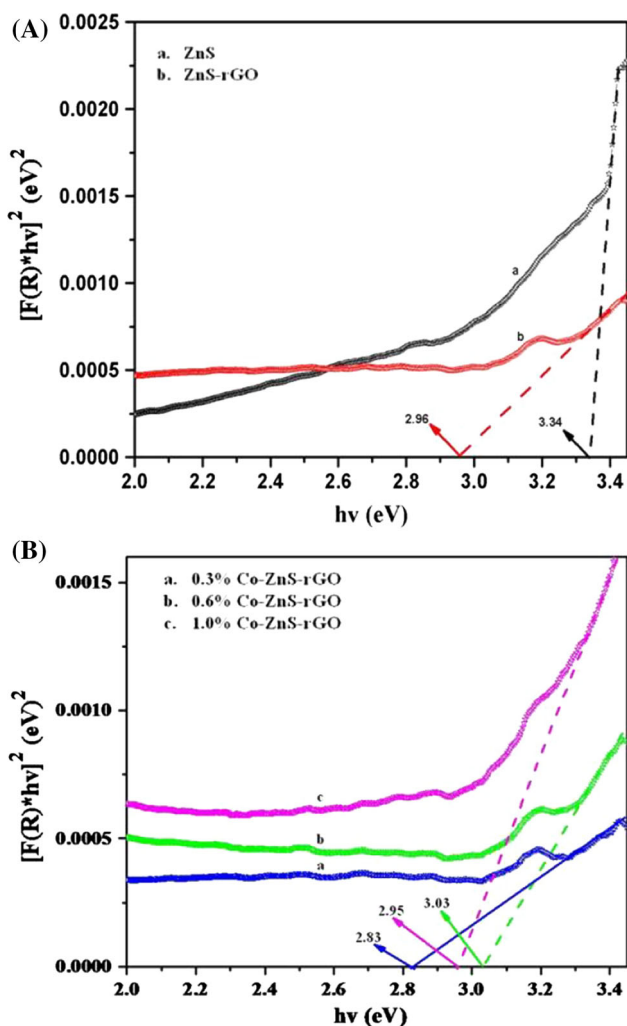Fig. 5 UV–Visible spectra of ZnS, ZnS–rGO and Co-doped ZnS–rGO with different concentrations of Co
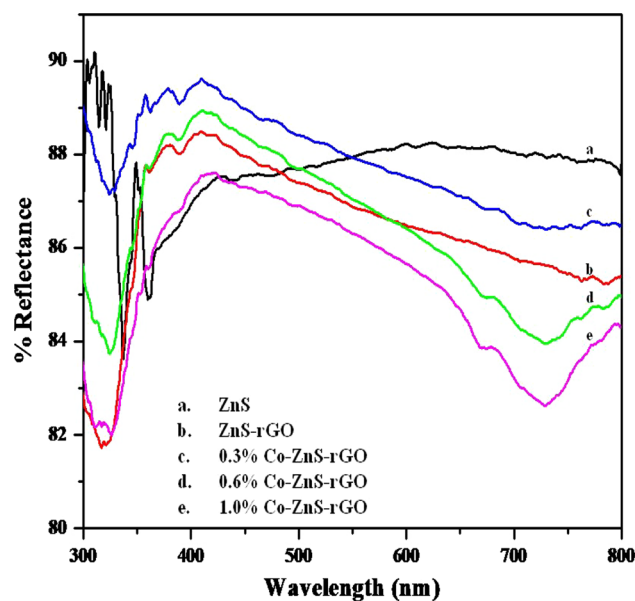
Fig. 6 UV–Visible diffuse reflectance spectra of ZnS, ZnS–rGO and Co-doped ZnS–rGO with different concentrations of Co

Fig. 7 Kubelka–Munk plots of ZnS, ZnS–rGO and Co-doped ZnS–rGO with different concentrations of Co

photo-excited by visible light irradiation. This restricts its photocatalytic activity in the UV region. The use of a photocatalyst in the visible light region is desired to harness the full potential of sunlight in photocatalysis. Figure 5a shows the absorption spectrum of the synthesized ZnS nanoparticle. From the spectrum it can be observed that the UV–vis absorption of ZnS showed a blue shift in absorption edge. The blue shift in the absorption edge arises from the quantum confinement effect of ZnS due to the presence of discrete energy levels [43]. As well-known, when the size of nanocrystals are relatively smaller than the exciton Bohr radius, quantum confinement effect could be induced and this can cause a shift of the energy level of the conduction and valence bands, hence, giving rise to a blue shift in the transition energy. However, the absorption spectra of ZnS–rGO (Fig. 5b) and Co-doped ZnS–rGO (Fig. 5c–e) nanocomposites showed significant increase in absorbance in the visible region. Thus the addition of rGO to ZnS has resulted in a red shift in absorption edge. Such red shift in absorbance in the visible light range is partly due to the fact that rGO serves as a photosensitizer for visible light absorption and also an electron reservoir to capture/shuttle the electrons photogenerated from the host ZnS [38]. Even though the ZnS–rGO showed an increase in absorbance in the entire visible light region, Co doping has further caused a significant increase in absorbance which decreased after $\sim\lambda730$ nm. An increasing amount of Co lead to higher absorbance in the visible region emphasizing the synergistic effect of rGO and Co in enhancing visible light activity of the semiconductor photocatalyst.

The UV–vis diffuse reflectance spectra for the as-prepared samples are shown in Fig. 6. Nanocrsytalline ZnS showed an increase in reflectance in the entire visible light region (Fig. 6a) whereas the ZnS–rGO and Co-doped ZnS–rGO samples showed a decrease in reflectance. This is due to the band gap excitation of electrons from the valence band to the conduction band due to the presence of rGO and Co. It can be observed that the absorption peak of

(A)

(B)

Fig. 8 Tauc plots of **a** ZnS and ZnS–rGO, and **b** Co-doped ZnS–rGO with different concentrations of Co

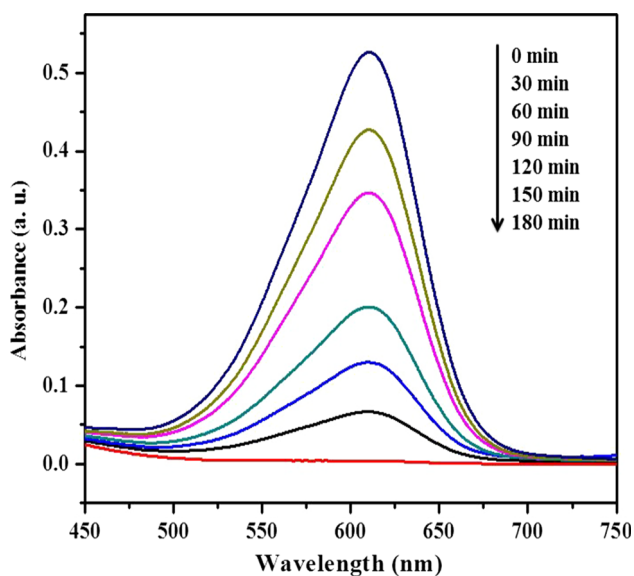**Table 2** Indirect band gap and percentage degradation after exposure to simulated solar light

Sample	Indirect band gap (eV)	Degradation (%)[a]
ZnS	3.34	10.5
ZnS/rGO	2.96	96.6
0.3 % Co–ZnS/rGO	2.83	100.0
0.6 % Co–ZnS/rGO	3.03	78.8
1.0 % Co–ZnS/rGO	2.95	91.7

[a] Measured after reaction for 180 min

versus hυ. For a direct allowed band gap semiconductor, the plot with n = ½ will show a linear Tauc region above the optical absorption edge. Indirect band gap materials show a Tauc region with n = 2 [44]. The value of the optical band gap can be calculated by extrapolating the Kubelka–Munk function to K/S = 0. Assuming an indirect band gap of all the samples, there is generally a gradual reduction in the band gap with the doped sample (Fig. 8). The obtained bandgap value for the ZnS was 3.34 eV and that of the doped samples ranged from 3.03 to 2.83 eV, with the 0.3 % Co-doped ZnS–rGO nanocomposite recording the smallest (Table 2). The relatively small bandgap of the 0.3 %Co-doped ZnS–rGO compared with the 0.6 and 1.0 % Co-doped samples may be due to the fact that as the concentration of Co increase in the host matrix, Co atoms act as electron trapping centers that result in a non-radiative recombination of electrons and holes. This means that the photoelectrons are preferentially transferred to the dopant level formed by Co doping, which become trapping centers [45]. As more Co enters the crystal lattice, sulfur ions are displaced creating native zinc vacancies. So in order to prepare a visible light active Co_xZnS_{1-x}–rGO with small bandgap, the relative amount of Co in the composite is very important to prevent electron–hole recombination.

3.7 Photocatalytic activity

The photocatalytic activity of the prepared ZnS–rGO and Co-doped ZnS–rGO nanocomposites was determined using the degradation of 20 ppm aqueous solutions of IC dye as a model for organic pollutants under simulated solar light. The optical absorption peak at 610 nm for IC was used to monitor the photodegradation process. The photodegradation performance of the ZnS–rGO and Co-doped ZnS–rGO nanocomposites showed an improvement in the rate of degradation of the dye compared with the bare ZnS nanoparticle. The spectral change in the concentration of the dye as a function of time during the degradation process for the 0.3 % Co-doped ZnS–rGO nanocomposite is shown in Fig. 9. With time increasing from 0 to 180 min, the

the synthesized ZnS nanoparticle, unlike the bulk (~320 nm) decreased clearly indicating a widening of band gap. However, the peak positions further shifted to a shorter wavelength due to the addition of rGO and Co.

The bandgap of the samples was determined using the Kubelka–Munk function:

$$F(R) = \frac{(1-R)^2}{2R} = K/S \tag{2}$$

where R, K and S are the reflectance, absorption and scattering coefficient respectively. The (K/S) spectra of the nanostructured ZnS, ZnS–rGO and Co-doped ZnS–rGO derived from the Kubelka–Munk function are shown in Fig. 7. The plots also show a red shift in the absorption coefficient of the ZnS–rGO and Co-doped ZnS–rGO photocatalysts.

For a semiconductor material, the Kubelka–Munk function allows the construction of a Tauc plot:$[F(R)*hυ]^n$

Fig. 9 IC photodegradation profile using 0.3 % Co-doped-ZnS–rGO

Fig. 10 IC degradation profile of ZnS, ZnS–rGO and Co-doped ZnS–rGO with different concentration of Co

characteristic absorption band at peaks of 610 nm decreased gradually, indicating that the IC was photodegraded by the catalyst. It was observed that the bare ZnS nanoparticles could only degrade *Ca.* 10.5 % of IC under the same irradiation time.
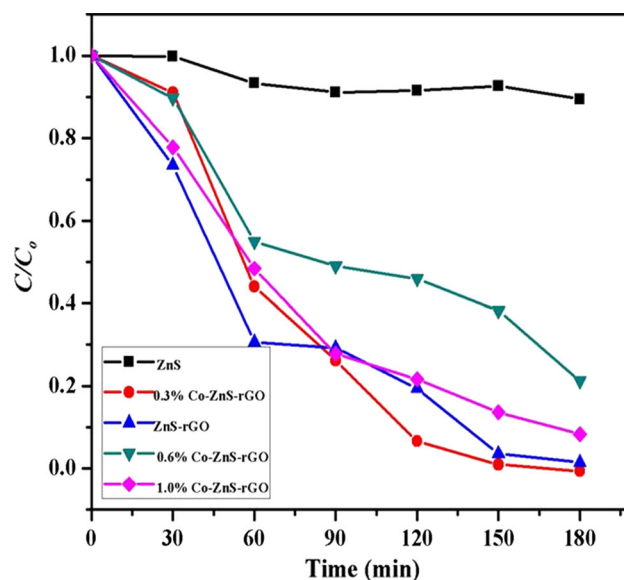
Table 2 displays the band gap and the percentage degradation of the photocatalysts. It is clearly seen that the 0.3 % Co-doped-ZnS–rGO showed much higher photocatalytic activity under visible light illumination. This is possibly due to the visible light absorption ability of 0.3 % Co-doped-ZnS–rGO photocatalyst as evidenced in the UV–visible and UV–visible diffuse reflectance spectra. An increase in the photocatalytic activity obtained in the case of the 0.3 % Co-doped sample is due to the ratio of Zn and Co in the nanocomposite which is efficient enough for the Co to act as an electron trap, retarding the electron–hole recombination. In addition to the small bandgaps, the rGO in the nanocomposites acted as a photosensitizer which accelerated the photocatalytic process compared with the ZnS nanoparticle [38].

In general, the photodegradation reaction of organic compounds can be described by the Langmuir–Hinshelwood model, where the photocatalytic activity of the photocatalyst can be evaluated using the equation:
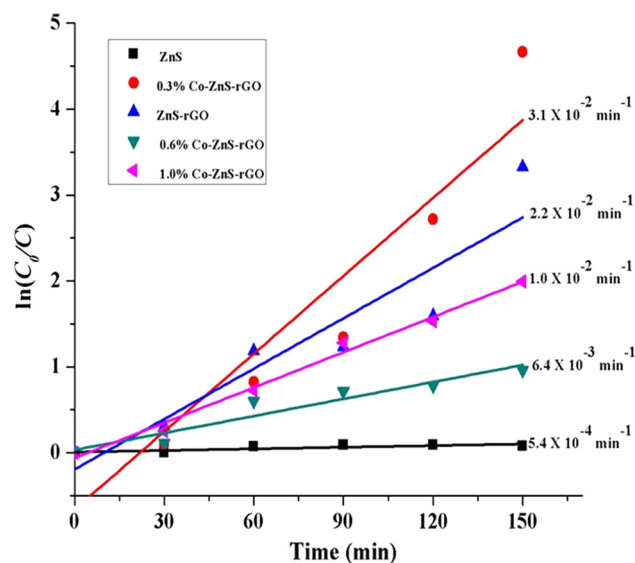
$$\ln C_o/C = kt \tag{3}$$

where C_o/C is the normalized IC concentration, t is the reaction time, and k is the apparent reaction rate constant.

Figure 10 shows the kinetics of IC degradation by plotting C/C_o vrs t. The ZnS–rGO and Co-doped ZnS–rGO nanocomposites show high degradation efficiency than the ZnS nanoparticles. The linear relationship of $\ln C_o/C$ vrs


Fig. 11 Kinetics of IC degradation in the first 150 min under visible light irradiation

t (Fig. 11) shows the photocatalytic degradation of IC by the catalysts. Fairly good linear relationships were obtained indicating that all the reactions followed pseudo-first-order kinetics. The rate of degradation of the dye was initially very fast for the ZnS–rGO up to 60 min but was faster for the 0.3 % Co–ZnS–rGO after 90 min. The value for k (Fig. 11) for the 0.3 % Co–ZnS–rGO which is 3.1×10^{-2} is more than fifty (50) times that of the ZnS nanoparticle. This shows that the rate of degradation by the

Scheme 1 Proposed visible light induced photocatalytic mechanism of Co-doped ZnS–rGO photocatalyst
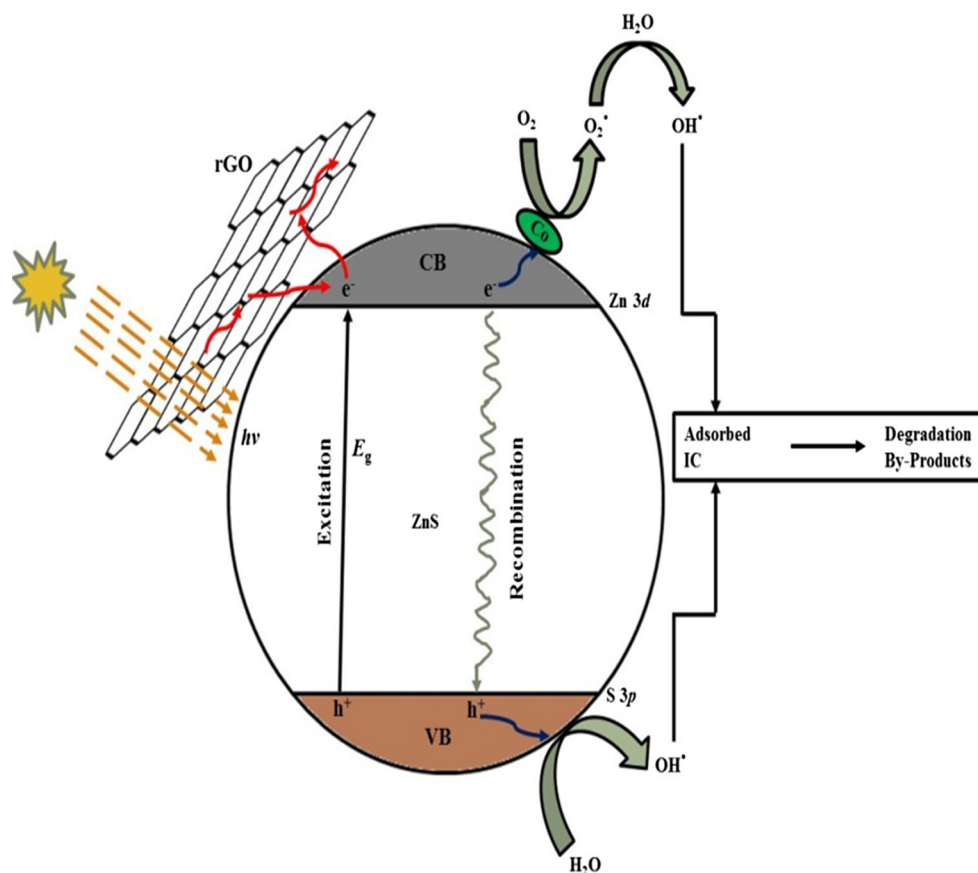
ZnS is several orders lower than the ones observed for the 0.3 % Co–ZnS–rGO nanocomposite. The better performance of the 0.3 % Co–ZnS–rGO nanocomposite could be explained by the synergistic effects of rGO and Co in the composite.

Co and rGO have synergistic effect on improving the photocatalytic performance of ZnS under visible light irradiation. Due to its wide band gap, it is difficult to excite an electron form the valence band (VB) to the conduction band (CB) of ZnS under visible light. The enhanced photocatalytic performance by rGO is due to its conductive structure which is believed to favor the separation of photo-generated electron–hole pairs by the formation of hetero-junction on the surface of ZnS. Under visible light illumination, rGO can acts as a photosensitizer by absorbing visible light which leads to excitation of electrons (e^-) from the VB to CB, creating holes (h^+) in the VB. Ideally, recombination of electrons and holes are expected. However, in the presence of rGO, photo-generated electrons may migrate freely towards the rGO surface. This leaves excess of valence-band holes on the ZnS that move to the surface and participate actively in the photocatalytic process. Scheme 1 shows the proposed visible light induced photocatalytic mechanism of Co-doped ZnS–rGO photocatalyst in which rGO acts as a photosensitizer and electron sinks.

On the other hand, in the presence of Co, the photo-generated electrons are trapped, leading to electron–hole separation. The holes can scavenge surface adsorbed water or hydroxyl molecules, generating highly reactive hydroxyl radical species. The electrons can scavenge the oxygen molecules to form very reactive superoxide radicals. Both hydroxyl and superoxide radicals are highly reactive towards the degradation of the dye molecule.

4 Conclusions

A simple co-precipitation method was used to synthesize visible-light active nano-crystalline ZnS–rGO and a series of Co-doped ZnS–rGO photocatalysts. XRD and TEM results showed that the samples were crystalline and consisted of mainly cubic ZnS phase. UV–visible spectra showed that both rGO and Co doping causes a red shift in the absorption edge of ZnS, which causes a significant reduction in the bandgaps. The highest photocatalytic activity was observed for the 0.3 % Co-doped ZnS–rGO sample. The bare ZnS showed the lowest photodegradation efficiency. The results showed that the control of Co doping in the nanocomposite is very important to prevent electron–hole recombination. The synergistic effect of rGO

and Co in the nanocomposites led to enhanced utilization of solar energy in photodegradation of IC dye through narrowing of band gaps.

References

1. M.M. Ayad, A.A. El-Nasr, J. Phys. Chem. **C114**, 14377 (2010)
2. P.C. Vandevivere, R. Bianchi, W. Verstraete, J. Chem. Technol. Biotechnol. **72**, 289 (1998)
3. D. Pak, W. Chang, Water Sci. Technol. **40**, 115 (1999)
4. G. Crini, Bioresour. Technol. **97**, 1061 (2006)
5. S. Chakraborty, M.K. Purkait, S.D. Gupta, S. De, J.K. Basu, Sep. Purif. Technol. **31**, 141 (2003)
6. P.S. Zhong, N. Widjojo, T.-S. Chung, M. Weber, C. Maletzko, J. Membr. Sci. **52**, 417 (2012)
7. M. Riera-Torres, C. Gutiérrez-Bouzán, M. Crespi, Desalination **252**, 53 (2010)
8. E. Ellouze, D. Ellouze, A. Jrad, R.B. Amar, Desalin. Water Treat. **33**, 118 (2011)
9. A.L. Ahmad, S.W. Puasa, M.M.D. Zulkali, Desalination **191**, 153 (2006)
10. M. Neamtu, A. Yediler, I. Siminiceanu, M. Macoveanu, A. Kellrup, Dyes Pigment. **60**, 61 (2004)
11. U. Bali, Dyes Pigment. **60**, 187 (2004)
12. M.S. Siboni, M. Samarghandi, J.-K. Yang, S.-M. Lee, J. Adv. Oxid. Technol. **14**, 302 (2011)
13. F. Zhang, A. Yediler, X. Liang, A. Kettrup, Dyes Pigment. **60**, 1 (2004)
14. M. Gao, Z. Zeng, B. Sun, H. Zou, J. Chen, L. Shao, Chemosphere **89**, 190 (2012)
15. S. Palit, Int. J. Chem. Sci. **10**, 27 (2012)
16. N. Kannan, M.M. Sundaram, Dyes Pigment. **51**, 25 (2001)
17. G. Mezohegyi, F.P. van der Zee, J. Font, A. Fortuny, A. Fabregat, J. Environ. Manag. **102**, 148 (2012)
18. A.R. Khataee, G. Dehghan, A. Ebadi, M. Zarei, M. Pourhassan, Bioresour. Technol. **101**, 2252 (2010)
19. I. Oller, S. Malato, J.A. Sánchez-Pérez, Sci. Total Environ. **409**, 4141 (2011)
20. C.-H. Wu, J.–M. Chern. Ind. Eng. Chem. Res. **45**, 6450 (2006)
21. S.J. Teichner, J. Porous Mater. **15**, 311 (2008)
22. X. Yang, F. Ma, K. Li, Y. Guo, J. Hu, W. Li, M. Huo, Y. Guo, J. Hazard. Mater. **175**, 429 (2010)
23. S. Choe, S.H. Lee, Y.Y. Chang, K.Y. Hwang, J. Khim, Chemosphere **42**, 367 (2001)
24. I. Matsui, J. Chem. Eng. Jpn. **38**, 535 (2005)
25. Y.W. Jun, J.W. Seo, J.O. Sang, J. Cheon, Coord. Chem. Rev. **249**, 1766 (2005)
26. S. Bhattacharyya, I. Perelshtein, O. Moshe, D.H. Rich, A. Gedanken, Adv. Funct. Mater. **18**, 1641 (2008)
27. A. Dev, S. Chaudhuri, B.N. Dev, Bull. Mater. Sci. **31**, 551 (2008)
28. G. Murugadoss, B. Rajamannan, U. Madhusudhanan, Chalcogenide Lett. **6**, 197 (2009)
29. J.H. Choy, H.C. Lee, H. Jung, S.J. Hwang, J. Mater. Chem. **11**, 2232 (2001)
30. W. Choi, A. Termin, M.R. Hoffmann, J. Phys. Chem. **98**, 13669 (1994)
31. E.I. Kapinus, T.I. Viktorova, T.A. Khalyavka, Theor. Exp. Chem. **42**, 282 (2006)
32. A. Ishizumia, C.W. Whiteb, Y. Kanemitsu, Physica E **26**, 24 (2005)
33. D.C. Marcano, D.V. Kosynkin, J.M. Berlin, A. Sinitskii, Z. Sun, A. Slesarev, L.B. Alemany, W. Lu, J.M. Tour, ACS Nano **4**, 4806 (2010)
34. M.J. Fernandez-Merino, L. Guardia, J.I. Paredes, S. Villar-Rodil, P. Solis-Fernandez, A. Martinez-Alonso, J.M.D. Tascon, J. Phys. Chem. C **114**, 6426 (2010)
35. R. Sahraei, G.M. Aval, A. Baghizadeh, M.L. Rachti, A. Goudarzi, M.H. Majles, Ara. Mater. Lett. **62**, 4345 (2008)
36. S.K. Mehta, S. Kumar, S. Chaudhary, K.K. Bhasin, M. Gradzielski, Nanoscale Res. Lett. **4**, 17 (2009)
37. K.K. Nanda, S.N. Sarangi, S.N. Shu, Nanostruct. Mater. **10**, 1401 (1998)
38. Y. Zhang, N. Zhang, Z.-R. Tang, Y.-J. Xu, ACS Nano **6**, 9777 (2012)
39. Z. Wang, B. Huang, Y. Dai, X. Zhang, X. Qin, J. Wang, Z. Zheng, H. Cheng, Cryst. Eng. Comm. **14**, 1687 (2012)
40. M. Salavati-Niasari, M. Randjbar, D. Ghanbari, J. Nanostruct. **1**, 231 (2012)
41. G.K. Ramesha, S. Sampath, J. Phys. Chem. C **113**, 7985 (2009)
42. E. Yoo, T. Okata, M. Kohyama, J. Nakamura, I. Honma, Nano Lett. **9**, 2255 (2009)
43. B. Barman, K.C. Sarma, Chalcogenide Lett. **8**, 171 (2011)
44. B.S.R. Devi, R. Raveendran, A.V. Vaidyan, Pramana-J. Phys. **68**, 679 (2007)
45. C. Bia, L. Pan, M. Xu, J. Yin, L. Qin, J. Liu, H. Zhu, J.Q. Xiao, Mater. Chem. Phys. **116**, 363 (2009)